Nanoscale

Accepted Manuscript

Volume 10
Number 4
28 January 2018
Pages 1549-2172

Nanoscale

rsc.li/nanoscale

ISSN 2040-3372

PAPER
Shuping Xu, Chongyang Liang et al.
Organelle-targeting surface-enhanced Raman scattering
(SERS) nanosensors for subcellular pH sensing

ROYAL SOCIETY OF CHEMISTRY

NCNST

This is an Accepted Manuscript, which has been through the Royal Society of Chemistry peer review process and has been accepted for publication.

Accepted Manuscripts are published online shortly after acceptance, before technical editing, formatting and proof reading. Using this free service, authors can make their results available to the community, in citable form, before we publish the edited article. We will replace this Accepted Manuscript with the edited and formatted Advance Article as soon as it is available.

You can find more information about Accepted Manuscripts in the Information for Authors.

Please note that technical editing may introduce minor changes to the text and/or graphics, which may alter content. The journal's standard Terms & Conditions and the Ethical guidelines still apply. In no event shall the Royal Society of Chemistry be held responsible for any errors or omissions in this Accepted Manuscript or any consequences arising from the use of any information it contains.

ROYAL SOCIETY OF CHEMISTRY

rsc.li/nanoscale

Vibrational and Nanoimaging of Eumelanin Superstructures modulated by Functionalized Micronized Graphene Oxide

Roberto Matassa[1,2,*], Sara Mattiello[1], Gustavo Guerreiro Candido Soares[3], Juan G. Lozano[4], Ana M. Beltran[4], Costantino Zazza[5], Nico Sanna[5], Jun Wei Phua[6], Jose Mauricio Rosolen[3], Andrea Di Cicco[1], Javad Rezvani[1], and Roberto Gunnella[1]

[1]Physics Division, School of Science and Technology, University of Camerino, 62032 Camerino, Macerata, Italy.

[2]Department of Anatomical, Histological, Forensic and Orthopaedic Sciences, Section of Human Anatomy, Sapienza University of Rome, Via A. Borelli 50, 00161, Rome, Italy.

[3]Departamento de Química, Faculdade de Filosofia, Ciências e Letras de Ribeirão Preto, Universidade de São Paulo, Av. Bandeirantes 3900, 14040-901, Ribeirão Preto, Brazil.

[4]Departamento de Ingeniería y Ciencia de los Materiales y del Transporte, Escuela Técnica Superior de Ingeniería y Escuela Politécnica Superior, Universidad de Sevilla, 41092 Seville Spain.

[5]Department for Innovation in Biological, Agro-food and Forest systems, Università della Tuscia (DIBAF), L.go dell'Università s.n.c., 01100 Viterbo, Italy.

[6]Insectta Pte. Ltd, 8 Cleantech Loop, Singapore, 637145, Singapore.

Corresponding authors: <u>roberto.matassa@unicam.it</u>, <u>roberto.matassa@uniroma1.it</u>

Abstract

Natural organic/inorganic materials with rational cooperative formations have long been of enormous interest owing to their hybrid self-assembling properties. Natural biomolecules are expected to produce attractive superstructures capable of sensing their environment, following its inherent biological functions and high biocompatibility. However, understanding their assembly strategies with inorganic material often poses a major challenge. Herein, we investigated the bioactive assembling of natural eumelanin superstructures modulated by chemical functionalization of the micronized graphene oxide to research their strong structural affinity by analysing their vibrational-structural correlations. The application of complementary experiments of high-resolution electron nanoimaging coupled with self-healing vibrational Raman spectroscopy revealed intriguing and unique features of this complex hybrid material. In particular, high

resolution nanodiffraction/imaging analysis evidence new nanocrystalline domains of pure natural eumelanin with different and irregular orientations forming irregular nanosheets. Interestingly, a disassembly and reassembly route of eumelanin units are actually evident not only on the oxide graphene surface but also located in high amounts on the edge of vertical graphene oxide, concretely supported by the analytical changes of the predominant resonance bands (*D, D***, and *G*). This confirms the ability of eumelanin to reassemble in spherical and elongated nanostructures induced by the external stimuli of the graphene oxide in aqueous solution at room temperature. This work thus highlights the assembling mechanisms for designing strategy to control bioactive molecules through environment modification.

1. Introduction

Living systems are abundant in oxygen, carbon and hydrogen organized in highly hierarchical structures. This complexity arise from the versatile chemistry of the carbon element, which enable the formations of superstructures held together by covalent bonds and/or the incorporation of oxygen-containing functionalities. These multidimensional superstructures of complex conformations, in particular the smallest biomolecular units, are known to be modulated through mutual interactions with their nanoenvironment, which is full of functional, flexible, and complex components.[1] This dynamic self-assembly commonly observed in biological-living systems can also appear in inorganic materials. One promising material platform is micronized graphene oxide (GO_m), since it has dimension and chemical composition similar to cells, bringing this inanimate material to the boundary between living organic and inorganic systems. The biocompatible graphene oxide surface exhibits high flexibility in forming biological-inorganic superstructures, enabled by localized functionalities at the atomic scale.[2] However, control over the contact interface is achieved using the simpler strategies, evolved in living systems, such as controlled assembly. This implies that an active biosystem capable of reacting to multiple inputs is dependent on both the binding of a small molecule and the engagement of functionalized carbon. One promising candidate is the pigment eumelanin (*e*Mel), abundant in nature and among the smallest active biomolecules. This melanin-like material shows broadband optical absorption, a useful property for human photoprotection, with some negligible minimum energy gap and low radiative quantum yield. Instead, eumelanin showed notable excitation energies at specific incoming wavelengths, yet its fluorescence is confined to a relative fixed energy range.[3] This relatively complex excitation-emission behaviour has been attributed to the poor long-range crystalline

order of the eMel molecules, as evidenced by wide- and small-angle X-ray diffraction studies, which yield diverse morpho-structural interpretations.[4,5] The possible existence of short-range crystalline order, not yet experimentally observed in eMel, may be associated with bifurcated hydrogen bonding, which is presumed to strongly interact with other hydroxyl systems (O–H···O), as theoretically suggested.[6]

The control over the chemical functionalization of eumelanin with the strong absorptive properties of GO_m substrates could result in the development of hybrid nanoscale device. Indeed, the assembly of possible sp^n hybridizations of this inorganic-biological system offers the opportunity to tailor electron-structural properties, enabling enhanced or combined mechanical strength, conductivity, and photon absorption over a wide range of wavelengths.[7,8] To make an impact on research and real technological applications, a key issue is the identification of high sustainable, low cost, and scalable production of the hybrid assembly processes, such as eumelanin extracted from the black soldier fly;[6 9] and the low-cost GO_m.[7] However, the removal of p_z orbitals from the π system in graphene oxide, which is manufactured by creating atomic vacancies or adsorbing functional groups in a controlled manner, remain a challenge. Indeed, the changing of the initial sp^2 hybridization to essentially sp^3, involving zig-zag edges, grain boundary, and atomic defects, experimentally appear to be randomly distributed on the GO_m sheets.[10,11] For these reasons, the morpho-structural arrangements of the modified graphene sheets, affected by bending, curving and wrinkling formations, have been characterized at the nanometric scale by direct microscopy imaging techniques.[12,13] Other indirect structural investigations, based on experimental and theoretical spectroscopies, revealed atomic defect sites on both surface and expanded edges that modulated the order/disorder of the sheet arrangements.[14,15] The interesting advantage of this layered material is the preserved threefold symmetry of the graphene atomic lattice, which favours physi-chemisorption of different active small species, in order to tune their hybrid physicochemical properties. A key issue for such applications is the determination of the possible hybrid interactions, in order to reveal the open opportunities and the limitations posed directly dependent on the size-spatial distribution of eMel on the two-dimensional structure of GO_m. Thus, expanding the study of micronized graphene oxide with the design flexibility of the organic eumelanin at both molecular and atomic levels remains a considerable challenge, broadening the scope of scientific research beyond traditional methodologycal investigations.[16] In particular, it remains unclear why the smallest structural units of eumelanin, such as a those with possible long-range and/or short-range ordered crystal lattices, often exhibit different nanometric

morphologies dependent on the extraction methods from different natural products.[17] Furthermore, a precise understanding of the short-range morpho-structural changes of eumelanin, which rearrange dynamically in response to the inputs, remains elusive.

For these reasons, the advancement of inorganic–biological synthesis approaches requires precise characterization techniques capable of revealing nanoscale details, in order to better understand the fundamental self-assembly mechanisms in inorganic–biological materials. Since the structural properties of hybrid materials are strongly dependent on size–shape, crystalline structure, and composition of the materials involved, an ensemble of electron microscopy techniques is necessary to fully characterize the morpho-structural properties of this inorganic–organic assembly. Despite being a powerful tool for structural characterization, the application of high-resolution TEM (HR-TEM) can induce radiation damage in a wide range of materials due to the exposure to the electron beam. Therefore, Raman spectroscopy may provide new insights into the atomic scale behaviour of the materials, overcoming the limitations of HR-TEM, and revealing the organic molecular structures and their interactions. Resonance micro-Raman scattering with high spatial resolution provides information about atomic defects as well as the order/disorder molecular stacking, which depends on the mutual orientation between crystal-size and polarization directions of the excitation wavelength.[18] However, the conventional vibrational Raman spectroscopy typically average information over much larger length scales, while the energy resolution remains unmatched compared to that of high-resolution electron imaging/spectroscopy. Therefore, the combination of localized atomic vibrations data with the morpho-structural data obtained by high resolution electron microscopy might provide a fingerprint for studying organic-inorganic-interactions.[19,20]

Herein, we report vibrational-structural analyses of the effect of changes in the eumelanin molecular organizations on the surface/bulk structural properties, influenced by the structural environment of defected micronized graphene oxide. This work aims at integrating morpho-structural-vibrational informations through a methodology designed to assemble small eumelanin units into superaggregates, an effect driven by the defects present in the graphene oxide layers, which can be used to tailor the optoelectronic properties of complex hybrid materials.[21] To obtain insight into these intriguing and complex hybrid biomaterials, a combination of Raman spectroscopy and electron microscopy imaging, supported by quantitative data/imaging analyses, has been used with the following objectives: (i) to investigate morpho-vibrational relationships in GO_m, eMel and GO_m-eMel by coupling TEM-Raman microscopy techniques (Figure 1), (ii) to

analyses the full morpho-structural properties of micronized graphene oxide, showing twisting, wrinkling, folding, and atomic defects formations (Figure 2), (iii) to image direct evidence of the short-range crystalline order in *e*Mel (Figure 3), (iv) and to monitor the changes in short-range order of the eumelanin molecular units modulated by oxygen-containing functional groups of defected micronized graphene oxide (Figure 4). Integrating the outcomes of the above scientific objectives in a synergistic way is crucial for understanding the directed assembly of novel nanoarchitectures through chemical functionalization and the hierarchical organization of biological materials with inanimate carbon structures.[22]

2. Results and Discussion

2.1 Morpho-vibrational behaviour from micron to atomic-length scale

Direct imaging of graphene oxide in micronized dimension (GO_m) revealed distinct interactions with eumelanin molecules, where structural reorganizations depend on surface and edge defects in GO_m. To gain insight into the self-assembly behaviour of the proposed inorganic-organic system at the nanoscale, high-resolution electron microscopy techniques (HRTEM, SAED, and EDX spectroscopy) were employed in order to obtain all comprehensive experimental findings (Figures 1-4). Further information on the presence of different oxidation interactions, structural defects and crystalline domains of such a hybrid system have been gathered using image analysis of nano-areas through sequences of Fast Fourier Transforms (FFTs) and Inverse Fast Fourier Transforms (IFFTs).[20,23]
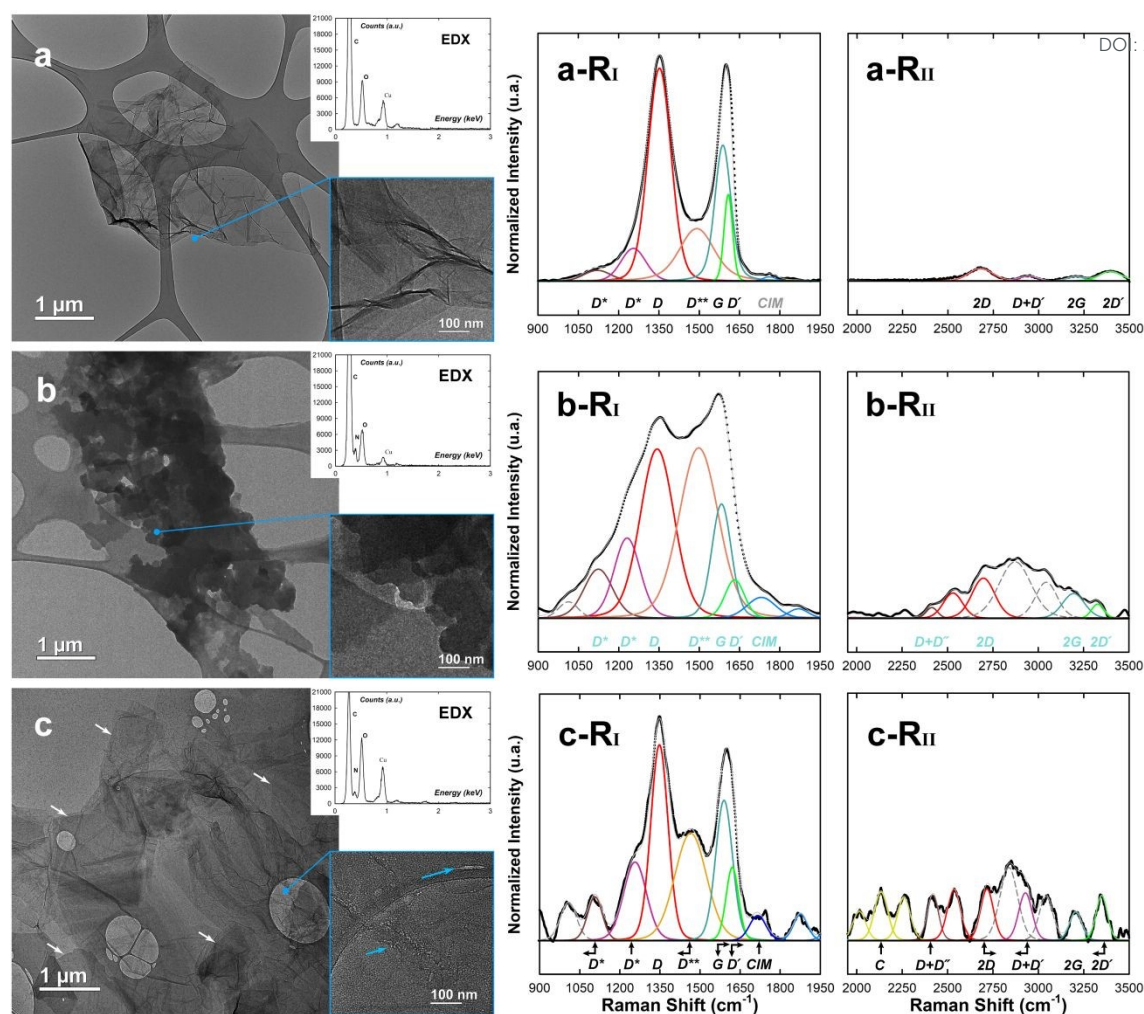
Figure 1. Morpho-vibrational microscopy of GO_m, *e*Mel and its interactions GO_m-*e*Mel species. a-c BF-TEM low magnification images of the GO_m, *e*Mel, and GO_m-*e*Mel, respectively. Inset: EDX spectra and magnified images of the corresponding compounds. a-c-R_I First-order resonance Raman spectra showing the experimental, fitting and its deconvolution profiles. a-c-R_{II} Second-order resonance Raman spectra showing the experimental, fitting and its deconvolution profiles.

However, due to the well-known limitations of high-resolution TEM to image the crystalline lattice of soft biomaterials, this technique needs to be combined with Raman spectroscopy at the atomic-length scale. These complementary experiments of conventional microscopies require an approach to integrate and analyze imaging-data to define the fine relationships between the structure and the essential interactions of these complex hybrid nanostructures. A first combination of these techniques with complementary spatial resolutions to understand the morpho-vibrational behaviors of micronized graphene oxide, eumelanin, and their hybrid interactions is summarized in Figure 1.

2.2 Direct vibrational-structural relationships in micronized graphene oxide

Bright-field TEM image of a GO_m sheet affected by bending, curving and wrinkling formations with highest electron transparent even in comparison to the thin-film carbon support is shown Figure 1a. Morphometric characterization shows the micronized nature of the GO_m with an area of 8.38

6

μm² and a planar dimension of about 3.79 μm. The O peak in the corresponding EDX spectra (Inset) confirms the presence of robust oxidation. The probed micro-Raman spectral region in the first-order ranging from 500 to 1900 cm^{-1} exhibits the typical D, G, and the hidden deconvoluted $D*$ and $D´$ bands (see in Figure 1a-R$_I$, Table S1). To study the chemical bond behaviours at the surface and edge, the D and G bands centered at 1.352 and 1.589 cm^{-1} typical of carbon derivatives arise from disordered graphitic materials and sp²-hybridized carbon system, respectively.[24] The D broad band, relatively intense compared to the G band, exhibits an estimated relative D-to-G intensity ratio of 1.09, implying the presence of short-range crystallinity order (Figure 1a) surrounded by atomic defects especially near the surface.[25] Indeed, the small crystalline planar size La of about 17.80 nm, inversely proportional to the intensity ratio, was estimated by including the experimental laser excitation energy.[15] The disorder-induced structure generated by irregular self-aggregation due to the hydrogenated and oxide carbon defects can be observe directly in the Inset of Figure 1a (see in Supplementary Information). Chemical-structural disorder coming from planar structural defects has been well-recognized in their different chemical vibration bonds by analysing the deconvoluted hidden peaks of the Raman spectra.[26] The middle band (D**) of a deconvolved peak at about 1491 cm^{-1} was estimated; in this in this context, such a band has been related to the edge plane of disorder pyrolytic graphite due to the (C=C) stretching of sp² hybridization and δ(C-H) bending modes of hydrogenated carbons.[27,28] The further D' band found at about 1608 cm^{-1}, partially merged with the G band arises from the C-O stretching modes at the edge, and from the surface hexagonal carbon rings generating short-range crystallinity order.[8] [11] Further bond vibrations of visible excitations obtained from the deconvoluted peaks at about 1129 and 1255 cm^{-1}, not measured in pristine crystal graphite, were observed in defected graphite and graphene oxide structures.[15] Both modes assigned to the $D*$ broad band have been assigned to the C-OH and C–C stretching vibrations of hydrogenated and not hydrogenated sp³ sites.[29]

Due to the broadening of first-order Raman peaks caused by atomic disorder—such as variations in bond lengths, bond angles, and functionalization—the Raman spectral range of the inorganic and/or organic species was extended to 2000-3500 cm^{-1} frequencies.[30] The identified combination between the fundamental modes are active in $D+D''$, $2D$, $D+D'$, $2G$, $2D'$ bands, providing information on the lattice dynamic of graphitized materials (Figure 1a-R$_{II}$, Table S1). The sum of the D'' and D modes, not detected in GO$_m$, can be associated to the $D+D''$ graphite band near 2462 cm^{-1}, as an identification of finite-size crystals (nano-islands).[27] [30] Among the measured overtone

peaks of the GO_m, the most intense-broad band exhibits a 2D band (2680 cm^{-1}), which confirmed the presence of turbostratic or twisted sheets, and therefore a low crystallinity order (Figure 2). This band represents an advantage to determine nanocrystal arrangements which may have not-defected twist assembling since the resonance of 2D and 2D' ($\sim$ 3393 cm^{-1}) peaks are independent from D peak. This is because the activation of two phonons with the same momentum is not required.[31] Instead, the combination of phonons with different momenta of the D+D' band ($\sim$ 2944 cm^{-1}), observed previously in graphene whiskers,[18] requires atomic defects for its activation.[14] Lastly, the overtone of the G and D' bands were assigned to the peak at about 3205 (2G) and 3395 (2D') cm^{-1}.

To confirm that the above mentioned signature of phonon modes is actually related to the presence of localized atomic carbon defects, high-resolution electron imaging of a single micronized GO sheet was carried out, and the results are shown in Figure 2a. In this regard, the bending, curving and wrinkling formations in the sheets, which are related to the resonance bands associated with disordered layers can be directly observed in Figure 2b. These puckered effects generate reduced structural coherence along the graphene surface due the random oxide-defect functionalization; which induce a broadening effect in the first-order Raman modes and weakening of the signal in the overtones modes (Figure 1a-R_I and -R_{II}). Indeed, the FFT pattern corresponding to an outer-nanoregion of Figure 2b-I shows superposition of two hexagonal patterns and other diffraction spots of weaker intensities due to the disorder in the layers stacking. The corresponding inverse FFT shows irregular waving dark lines at the edges separated by 0.39 nm, larger than the interlayer spacing in pristine graphite (0.33 nm), suggesting that there are four waved hexagonal planes. Interestingly, the wavy morphology of the folded sheets affects the resolution of the crystalline lattice fringes between the edge and the stacked layers (red dot line); whereas the inner region clearly shows crystalline lattice with Moiré pattern due to twisting layers formation. In addition, farther from the edge, the high intensity of the FFT spots evidences a superimposed 4 layers rotated of 17.3° around [002] zone axis (Inset) and the corresponding IFFT images shows lattice spacing of 0.209 nm, belonging to the (101) reflection plane (Table S2). These direct imaging evidences of bending and twisting in the layers are highly consistent with resonant Raman mechanisms (2D Band, Figure 2a-R_{II}).[32]
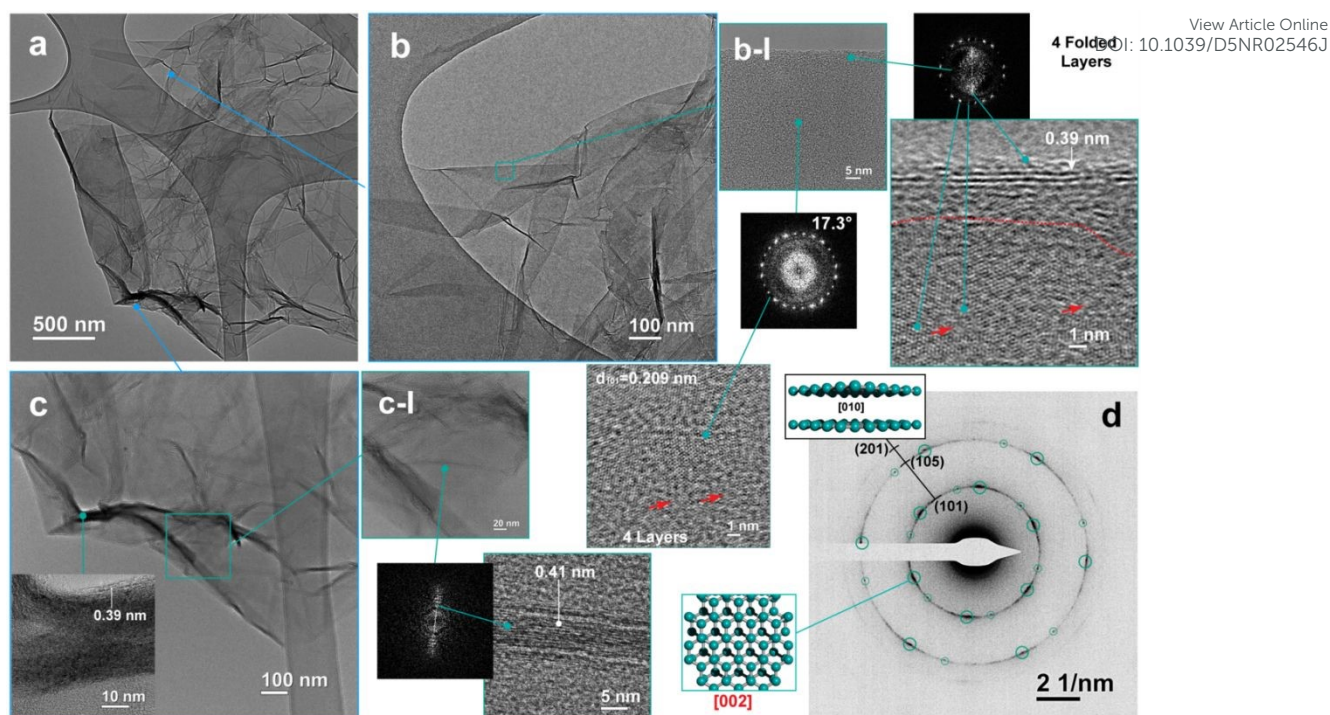
Figure 2. Morpho-structural observations of GO_m bending, curving and wrinkling formations. a BF-TEM image of graphene oxide sheet. b High magnification of the GO_m edge (blue square of a). b-I High resolution image of nano-area of b (green square). Insets: the corresponding FFT patterns of GO_m hexagonal shape (green dots) over their IFFT images (bottom and right sides). The bottom IFFT image of nanometric area illustrating crystalline lattice fringes partially disturbed by oxidation interactions (red arrowed). c High magnification of the disordered flakes. c-I High resolution image of nano-area of c (green square). Insets: vertical multi-layers graphene; high resolution image of nano-area of c (green square, left top side); an IFFT image of nanometric area (green dot) illustrating large crystalline lattice fringes of vertical GO_m. d EDP taken from a showing distinct rings and diffraction spots belonging to the P63/mmc hexagonal symmetry of graphite phase.

Furthermore, the disturbed twisted crystal structures with the presence of island coalescence formation attributable to strong oxidation interactions (red arrowed, IFFT image of Figure 2b-I) are displayed at high resolution and analytically measured by the vibrational atomic defects (*D** and *D'* Bands, Figure 2a-R_I). High-resolution imaging of the curving and wrinkling effects is displayed in Figure 2c. The curved lattice fringes show a spacing of about 0.39 nm which decreases to reach densely packed sheets of dark intensity (Inset, bottom left). This may be attributed to the high amount of hydrogenated sp^3 sites also detected by the resonance *D** band. Similarly, the bending, curving, and wrinkling formations of both basal and edge sheets are shown in Figure 2c-I (green square). The corresponding IFFT image shows an interlayer spacing of 0.41 nm of a possible vertical and expanded sheet edge with dark intensity contrast compared to the surface layers. The presence of vertical edges is also confirmed by broadening behaviour of the *2D* band, which is generated by the polarization direction of the excitation beam, perpendicular to the abundant defected vertical sheets.[18] The opening effects of the micro-sheets due to a possible intercalation

of the oxide groups can be related to the measured slight blue-shift of the G_{GOm} band, previously reported.[33]

Complementary to this, we recorded electron diffraction pattern (EDP) to validate the vibrational data discussed above. Figure 2d shows the superposition of two EDPs. By measuring the d-spacing of the diffraction rings produced by a random orientation of the GO_m layers, the P63/mmc hexagonal symmetry with preferential crystallographic orientation (101) and higher-order diffraction rings (105 and 201) has been identified. The relevant and concomitant absence of (002) planes indicates that GO_m planes intercept perpendicularly the crystallographic b-axis (axis parallel to the layers, zone axis [010]), which is an experimental confirmation of the presence of the exposed sharp edge of vertical GO_m. The second EDP of ordered diffraction spots with irregular intensity has been identified to belong to the six-fold symmetry with hexagonal structure of AB stacking order (green circles), intercepting perpendicularly the crystallographic c-axis (or stacking axis of graphene layers, zone axis [002]), confirming the analysis of Figure 2c. These findings confirm that the turbostratic and twisted character of the micronized graphene oxide arise from the presence of highly active defected, ideal for a higher catalytic activity.[13]

2.3 Direct evidence of eumelanin nanostructures of having a vibrational broad signal

Morphological observations of the *e*Mel biomolecule have shown nanostructured microaggregates sheets-like of irregular shape and size with high roughness edges (Figure 1b), and the chemical species present have been confirmed by EDX spectroscopy (C, O and N; Inset). The corresponding Raman *e*Mel spectra consisting of broad bandwidths with two main resonant peaks (1343 and 1583 cm^{-1}) suggests a structural disorder of the molecular orientations, having a similar Raman profile to other natural eumelanin (see in Figure 1b-R_I, Table S1).[17] The peak at approximately 1343 cm^{-1} has been assigned mainly to the ν_{as}(C-C) asymmetric stretching modes of the indole-atom rings (less resonance for ν_{as}(C-N) mode), and to the in-plane δ(O–H) and δ(C–H) with dominant bending.[34] The ensemble of these vibrational modes, aligned in frequency to the D band of the GO_m, can be related to the indole π-π interaction stacking factors of vertical missing orientation of the *e*Mel units, showing indeed high roughness near the surface sheets (Inset of Figure 1b). The second dominant peak at approximately 1583 cm^{-1}, close to the G_{GOm} band frequency position, has been mainly attributed to the predominant ν_s(C=C) *symmetrical* stretching mode of the phenol ring, similar to the sp^2-hybridization of the carbon oxide system, coupled with in-plane δ(O–H) mode. The slight red-upshift of the G_{eMel} band, compared to the GO_m spectra, arises from the larger contribution of the vibrational density of states of the isolated sp^2 phenol

Nanoscale Accepted Manuscript

rings. And the in-plane δ(O–H) mode contribution of eMel molecules is more than for graphene oxide sites which has high surface area to volume ratio. Indeed, the eMel intensity ratio $I_{D/G}$ (0.91) was less than the GO_m because of a special enhancement factor in graphene oxide on the D_{GOm} mode in the presence of bending and whisker formations, followed by increasing crystalline planar size La of about 21.13 nm for eMel. Similar to the sp^2 hybridization stretching of the GO_m, the middle D^{**} at about 1476 cm^{-1} has been revealed and assigned to the main v_{ring}(C=C) *asymmetric* stretching mode of the six-atom rings coupled with in-plane δ(O–H) bending mode.[35] The broader and up-shifted D^{**} band, compared to GO_m, is a peculiar signature of large vibrational resonance of the carbon and oxygen atomic bonds of the eMel units, having a great amount of different orientations to the excitation polarization direction. The vibrational peak at about 1632 cm^{-1} has been assigned to the C-O stretching mode similar to the GO_m contribution. The vibration of the out of-plane γ(C=C) and γ(O–H) bending mode of the pyrrole structure (~1124 cm^{-1}) can be related to the stretching vibrations of both hydrogenated sp^3 sites, similar to the D^{*}_{GOm} band. The vibrational peak at about 1231 cm^{-1} has been related to the v_{rings}(CNC) symmetric stretching modes and in-plane δ(O–H), δ(N–H), and δ(C–H) bending modes.[17] These results evidence that the Raman spectrum originated from both the pyrrole and indole rings coupled with the hydroxyl group, generating different bond strengths and vibrational frequencies, all very close to turbostratic graphite oxide flakes.[36] The remaining first-order vibrational peaks at about 1719 and 1869 cm^{-1} are assigned to the v_{as}(C-N) and v_s(C=C) stretching modes coupled with in-plane δ(N–H), δ(C–H) and δ(O–H) bending modes of the indole rings, respectively. Additionally, there are a series of second-order bands, assigned mainly to the C-H stretching mode, that are active near the *2D*, *2G*, *2D'* bands of the GO_m (2697, 3195, and 3327 cm^{-1}, Figure 2a-R$_{II}$). Similarly, the vibrational peaks at about 2419 cm^{-1} can be associated to the $D+D''$ graphite band, as an identification of finite-size crystals (nano-islands).[31] The $D+D'$ band could not be assigned because of the absence of atomic defects for its activation. Instead, two deconvolution peaks are measured (2873 and 3043 cm^{-1}). To date, significant efforts have been devoted to theoretical research aimed at predicting the structure of eumelanin, comparing its broad Raman bands with well-known organic systems. However, these valuable outcomes lack crucial connection between the vibrational atomic-lengths and the experimental structures under study. Thus, understanding how self-assembling processes generate short-range organized structures is essential for developing strategies to control the physico-chemical properties of these biosystems. The use of low dose high resolution electron imaging has allowed a detailed analysis on self-assembling eumelanin in Figures 3a-c.[19,37]
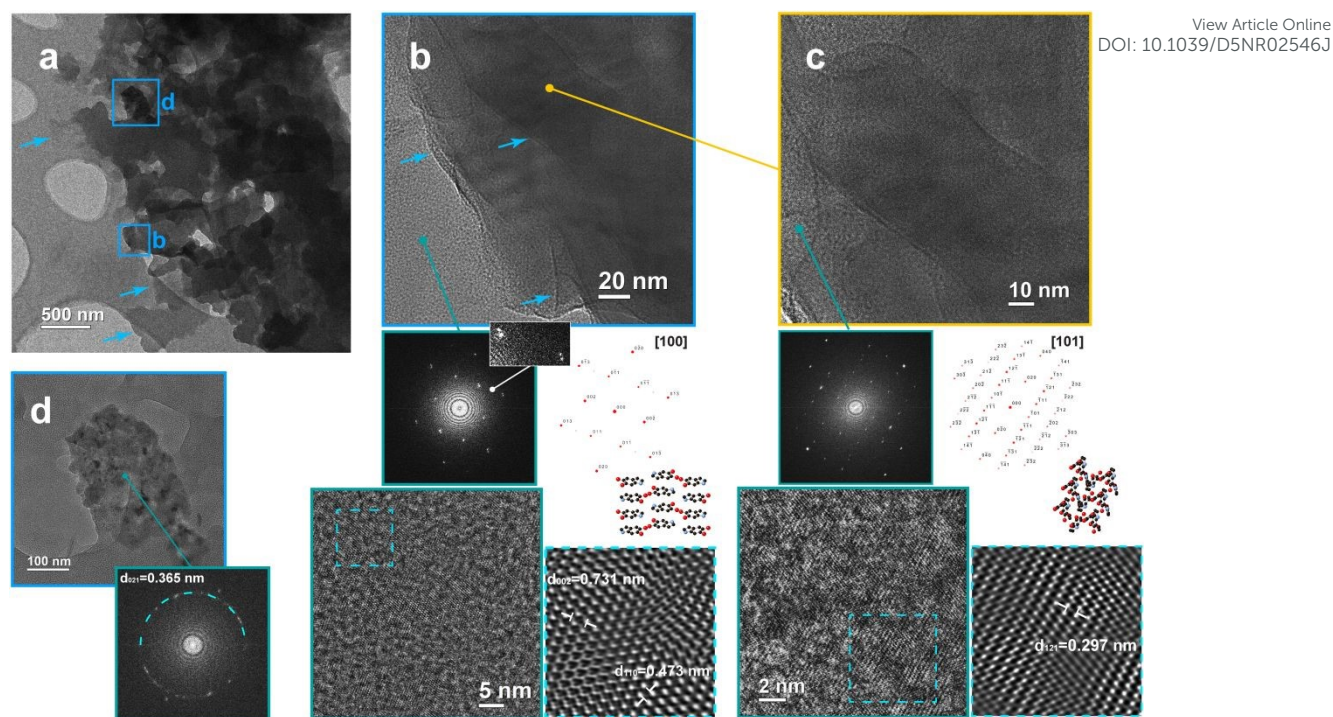
Figure 3. Morpho-structural observations of self-aggregations of eumelanin molecules. a BF-TEM image of eumelanin irregular nanosheets (blue arrows). b High magnification image of the eumelanin layers (blue square of a). Insets: FFT spot pattern of ultrathin eumelanin with quasi-hexagonal shape (green spot-line) and smallest inset showing extra array of diffraction spots; identification of FFT diffraction spots by electron diffraction simulation with [100] zone axis of crystalline eumelanin (below FFT image); high resolution IFFT image of nanometric area illustrating crystalline lattice fringes (beside FFT image); an amplitude-filtered single frame that is produced by inverse of the IFFT image and crystalline eumelanin structural model below. c High resolution image of eumelanin in the thin region of b (green spot-line). Insets: FFT spot pattern of c and its corresponding electron diffraction simulation with [101] zone axis; high resolution IFFT image of nanometric area (green square of c) and its amplitude-filtered single frame illustrating zig-zag atomic organization confirmed by structural model below (cyan dot-square). d High magnification imaging of the eumelanin layers (blue square of a) and its corresponding FFT ring pattern of thick eumelanin (cyan dot -arc).

Bright-field TEM images of eMel reveal irregular micrometric layers with regions of both low and high electron transparency, in contrast to the continuous and transparent micron-sized sheets observed in the defected GOm (Figures 3a and 2a). This variation in intensity contrast arises from the disordered stacking of self-assembled nanosheets with irregular shapes, shown in Figure 3a-b (blue arrows).The used imaging method, which is analogous to nanodiffraction, has identified for the first time different structural behaviours of eMel molecules in two nanoregions of the Figure 3b. The FFT pattern, showing quasi-hexagonal diffraction spots suggests the presence of ultrathin layers of eumelanin laying on the holey carbon amorphous thin-film support. The FFT pattern has been compared to the electron diffraction simulation from a crystal built considering the space group $P2_12_12_1$ using the unit-cell parameters calculated by DFT theoretical model;[38] which is in agreement with the presence of a molecular layer of eMel oriented along the [100] zone axis parallel to the electron beam. Moreover, an extra array of diffraction spots is present in the FFT

pattern (Inset of FFT, top right side), indicating a missing orientation of the stacked molecular units along the transversal crystalline plane orthogonal to the [100] zone axis. Indeed, the corresponding IFFT image below shows crystalline lattice fringes with different orientations, indicating short-range order of nanoregions. This finding can be seen more clearly in the amplitude-filtered single frame generated by the inverse of the FFT image (beside) in which lattice fringes have large spacings of 0.731 nm (002) and 0.473 nm (110) compared to the crystalline lattice of GO_m (Table S2). The visible quasi-hexagonal crystalline shapes might be related either to the stacking tilt or disorder of the eumelanin units that validate the measured broad bands at about 1343 cm^{-1}. The hypothesis of vertical missing orientation of the eMel units attributed to the so-called D_{eMel} band has been also confirmed by analysing another region. By performing FFT scanning in Figure 3c, a nanoregion shows a further pattern of well-organized diffracted spots (green square, and below of Figure 3c). The electron diffraction simulation identified a different preferential orientation of eMel molecules oriented along the [101] zone axis; wherein the IFFT image shows a zig-zag shape of assembled eumelanin with crystalline lattice of spacing 0.209 nm (blue square of Figure 3c). This particular shape, not visible in the other near nanoregions, might be related to the edge roughness of eMel nanosheets measured by the inducing-disorder D and 2D bands, similar to graphitic materials.[15] It is interesting to notice that the change in the crystalline orientations into two different nanoregions (amorphous carbon [100] and eumelanin bulk [100] zone axes) evidence the ability of smallest biomolecule to be structurally modulated by external environmental interactions. This is consistent with the measured broader and up-shifted D^{**} of the eMel nanosheets, confirming the different crystalline orientations under the excitation polarization direction. Indeed, a thick region of eumelanin, showing missing layer formation, still evidences the nanocrystal character of random orientation, confirmed by the derived FFT pattern of Figure 3d (blue square of Figure 3a). This actually confirms the presence of nano-crystalline planes with a high degree of randomly orientated nanostructured complexes of varying units; which might be related to irregular monomer and functional group arrangements of the eumelanin. Therefore, the changing dimension and orientation of the crystalline nanodomains had a strong impact on the phonon modes, in that the series of eMel superstructures with random orientation ($[h,k,0]$) and random stacking ($[0,0,l]$) along the crystallographic axes, broadening the Raman spectra (Figure 2a-R_I and -R_{II}).

2.4 Vibrational and nanoimaging of hybrid biocompatible superstructures

To understand how biomolecular structures may be affected by external nano-environments of an inanimate defected structure, eumelanin molecules were hybridized with the carbon oxide system, shown in Figure 1c. The micrograph shows overlapping of micronized multilayers affected by bending, curving and wrinkling (indicated by white arrows). A magnified nanoregion of the GO_m sheet shows high surface roughness due to the presence of nanostructured-objects which have slightly brighter contrast, self-organized in aligned and isolated nanoparticles (marked with blue arrows, Inset of Figure 1c), not observed in GO_m (Figure 1a). The EDX spectra shows a more intense oxygen peak, compared to GO_m alone, and a well-defined nitrogen peak related to the observed organic biomolecules (Inset of Figure 1c). This first observation evidences the ability of the smallest eMel to change structurally and morphologically from irregular nano-sheets into nanoparticles, after interacting with disorder-defected micronized GO (Figure 2).

The corresponding Raman spectra shows similar broad bandwidths of the GO_m spectra profile with overlapped peaks of the eMel Raman, evidencing a limited excess of eMel during the sample fabrication. The first-order peaks of the Raman signals (*D**, *D*, *D***, *G*, *D´* and *CIM* bands) exhibit slight changes in intensity-position-width (Figure 1c-R_I); while the second-order Raman peak profile evolved with a gradual narrowing of the overtone bands (Figure 1c-R_{II}). By excluding spurious peaks due to the excitation frequency (532 nm) used, the G band shows a slight downshift towards a higher frequency in GO_m-eMel (1592 vs 1588 cm^{-1}) in spite of the high-intense-broad G_{eMel} band, followed by narrowing of the D band profile. These resonance scattering behaviour may be attributed to the following competing mechanisms: structural-vibrational reorganization with decreasing doping level compared to defected GO_m; active phonons modes at high frequency due to their confinement of the isolated (C=C) and (O-H) shorter bonds of the smallest biomolecules; atomic reorganization induced in the sp^2 carbon lattice through eMel epoxy and hydroxyl groups, which would mean that a chemical functionalization does indeed occur.[26] However, only a slight decrease of the crystalline planar size *La* of 16.47 nm (I(D/G) 1.17) was estimated, indicating a decrease in crystallinity orientations then a phonon propagation in the GO plane, parallel to the polarization direction of the excitation beam. The crystallinity decrease of this hybrid product might also be correlated to the ascertain interaction of eMel units with GO_m, which may reduce the latter's reactive oxygen functionality.[10] In this regard, the prominent *D*** band at about 1463 cm^{-1} red-shifted upwards to that of sp^3 hybridization of the pristine GO_m may be related to increasing of tetrahedral carbon species, generating an augment in conformational disorder with nanometric formations of bio-carbon allotropes. Therefore, the strong interactions

of the (O–H) bending mode may be attributed to strong cooperation between eMel and the atomic oxidized defected GO_m, especially on the edge plane (Figure 4b).

The dominant middle $D**$ band in the GO_m was also assigned to the formation of spherule carbon structures,[38] comparable to our observations of spherule eMel nanoparticles in the Figure 4c and in the inset of Figure 1c. Indeed, the measured broad and blue-downshifted D' band (1625 cm^{-1}), assigned before to the (C-O) vibrational stretching in GO_m, still evidences the presence of biomolecule interactions with vacancy defects on the GO_m surfaces.

The strong interactions between GO_m-eMel are evidenced by an increased intensity of the $D*$ band, with well separated modes (1107 and 1255 cm^{-1}), which confirms the increased C–C stretching vibrations of both hydrogenated and unhydrogenated sp^3 sites. This hybridization character of covalent interactions between spherical and sheet-like carbon biostructures may be evidenced by the increased intensity modes at about 1719 cm^{-1}, and the peak of 1876 cm^{-1} which was not measured for GO_m. These Raman peaks, attributed to the Stone-Wales defects,[26] have previously shown similar resonance vibration (1830-1880 cm^{-1}, CIM-Band) in a monodimensional carbon system interacting with the surface of different carbon species.[40] Indeed, high resolution TEM observations of Figure 4c (blue arrowed) evidence linear self-aggregation of eMel nanoparticles that interact with the aligned defects along the lattice fringes of wrinkling or puckered GO_m sheets, shown in Figure 2c-I.

These findings have been also confirmed by comparing the second-order resonance Raman spectra. The GO_m-eMel exhibited well separated and high-intense peaks compared to the eMel and GO_m spectra (Figure 1c-R$_{II}$). The asymmetric shape of the shifted-up $D+D''$ band ($\sim$ 2419 cm^{-1}) indicates a change in the electronic structure within the conduction bands for increased n-layers of different combination phonon wave vectors.[41] This scattering process, slightly measured in eMel spectra, can be further related to the presence of biomolecules units organized in ultrathin elongated nanosheets of finite-size crystals (nano-islands),[31] laying on the GO_m surface (Inset of Figure 1c). Interestingly, a double-resonant scattering process exhibited a stronger and narrower 2D bands splitted in two deconvoluted peaks (2535 and 2719 cm^{-1}), one of which was blue-shifted upwards in comparison to that of GO_m (2680 vs 2719 cm^{-1}). These two dominant subcomponents have been assigned in graphene to be related to the increasing number of intercalant layers due to the splitting of electronic bands and phonon branches.[33,42] A further presence of non-aromatic CH groups has been attributed to the spectral region 2800-3000 cm^{-1}, having strong-broad band splitted in three deconvolution peaks identified at about 2837, 2928, and 3048 cm^{-1}. The

measured D+D' band, red-shifted upwards to that of GO_m (2944 vs 2928 cm^{-1}), was related to the interesting decrease in reduced atomic defects at the edge of graphene whiskers.[13,18] The appeareance of C peaks, composed of three peaks at about 2014, 2156, and 2252 cm^{-1}, not measured in GO_m and in eMel, provide evidence for further interlayer hybridization, assigned to the stretching modes of sp hybridized carbon of inducing carbine formation from polymers or hydrocarbons.[43] In addition, the high-frequency 2G and 2D' bands (3205 and 3349 cm^{-1}) have been assigned to the stretching vibration of hydroxyl (C–OH) groups.[24]

High resolution imaging clearly shows the self-assembling hybrid interactions of GO_m-eMel with different intensity contrast of a few layers in Figure 4a. The puckered GO_m-eMel sheets, shown in Figure 4b (blue arrowed), displays irregular and widest lattice fringes of nanostructured eumelanin linearly distributed along the direction of the curving and exposed edges of the graphene oxide, not observed in the pristine GO_m (Insets of Figure 2c). This strong interaction of the GO_m-eMel system may most likely be related to the doping/intercalation with increasing layer numbers and a decrease in the reactive oxygen functionality of GO_m. Indeed, this has been confirmed by the sensitive Raman spectra through a blue-shift of the G and 2D bands with narrowing of the $D_{GOm\text{-}eMel}$ band (Figure 1c-R_I and -R_{II}). Yet from nanoparticle formations perspective, spherule eumelanin structures appear with bright intensity contrast compared to the dark GO_m sheets in Figure 4c, showing bright isolated and aligned nanoparticles of about 3-9 nm in width along the puckered GO_m sheets (blue arrowed). This remarkable structural change of the pure eumelanin, extracted from the black soldier fly, previously assembled in irregular nano sheets, and now reassembled in spherical nanoparticles with GO_m, could imply that the molecular units are noncovalently linked without polymeric conformations. The allocated nanoparticle/oxide-layer interactions, similar to the spherule carbon structures, are validated by the prominent red-shifted D^{**} band. The bright aligned nanoparticles, anchored on the GO_m surface, are validated by the appearance of second-order C stretching mode (interlayer sp hybridization) and the increased CIM band (1D-carbon surfaces with carbon species). The interesting reduced atomic defects of GO_m due to the interactions with eMel is also confirmed by the slight red-shift of the D+D' band. These complementary findings suggest that eumelanin molecules are capable of multiple dynamic nano-organizations, and mutually interacts with the atomic defected GO_m edge, forming interesting nanoaggregates.
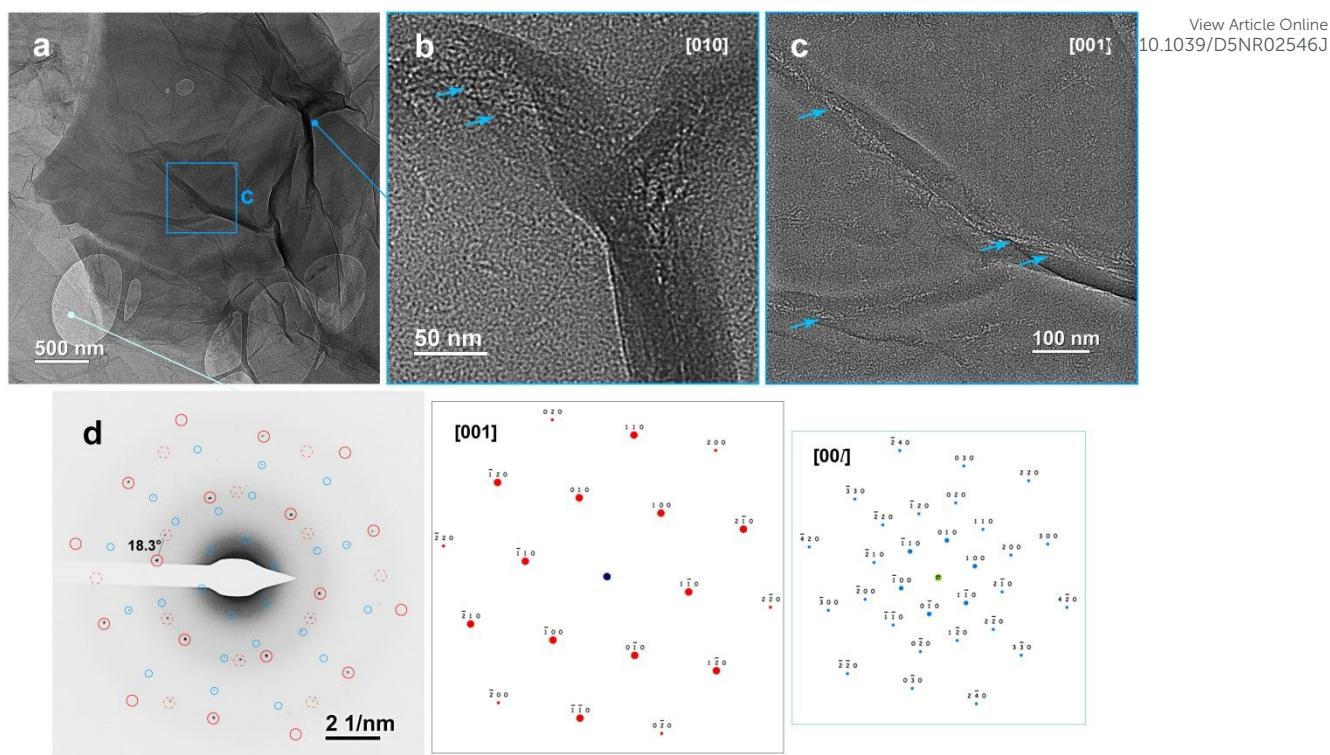
Figure 4. Morpho-structural observations of eumelanin interacting with graphene oxide sheets. a BF-TEM image of graphene oxide sheet. b High resolution image of the eumelanin bright nano-aggregates (blue arrowed), interacting on the edge of vertical graphene oxide. c High magnification of nano-area of a (blue line) showing bright nano-aggregates of eumelanin aligned along the defected GO_m sheets (blue arrowed). d EDP taken from a showing distinct diffraction spots belonging to the P63/mmc hexagonal symmetry of graphite phase (black circles) and to the space group $P2_12_12_1$ of crystalline eumelanin (blue circles).

The low-dose experimental electron diffraction displays two superimposed diffraction patterns (Figure 4d). The diffraction spots of sixfold symmetry of bilayer graphene have been indexed according to the structure of graphite with space P63/mmc (black arcs, d_{001}= 0.339 nm) and behind the corresponding simulated EDP with zone axis [002], already detected in the EDP of the pristine GO_m (green circles, Figure 2d). A second stack, still present after *e*Mel interactions, is rotated approximately 18.3 degrees around the [002] zone axis (black dot circle), in agreement with the corresponding intense 2D Raman band. Interestingly, additional spots, closer to the central stop, exhibits a further sixfold symmetry with first-order hexagonal spots more intense than the high-orders, confirming the presence of a further layer in staking configuration.[44] The measured *d*-spacing of 0.776 nm is slightly higher than the (001) crystallographic plane of crystalline eumelanin with the space group $P2_12_12_1$. Therefore, the increased interlayer spacing between GO_m sheets along the crystallographic stacking *c*-axis may be attributed to an organophilization of the eumelanin molecules through the reduction of oxidized carbon functional groups on the basal planes and edges of GO_m.[45] Yet from complementary perspectives, this is in agreement with hybrid intercalated layer formations inducing random stacking ($[0,0,l]$) along the

17

crystallographic *c*-axis, such that the narrowing 2D increment and D modes does indeed occur (Figure 1c-R$_I$ and -R$_{II}$).[42,46] Moreover, the occurred re-organization of the vacancy defects due to the doping/intercalation variation is in agreement with the shift G and D' bands to high frequencies.[33] This strong covalent interaction between spherical/sheets carbon biostructures has worked also like a functionalization/reduction of coverage oxidation product at the atomic defects of GO$_m$, that might result in an increase in conductivity.[9]

3. Conclusions

Our work presents experimental imaging/analytical evidences that challenges traditional understandings of self-assembling behaviour of eumelanin superstructures, depending not only on the contact area but also on the shape of domain engagements. Indeed, we demonstrate that interfacial contacts of the micronized graphene oxide sheets cause effective morpho-structural changes in eumelanin, from their naturally occurring irregular short-range order domains to form diverse superstructures with the biocompatible carbon oxide substrate. The experimental approach demonstrates the efficacy of using conventional vibrational resonance micro-Raman and high-resolution electron microscopies, which complement each other in determining the morphologies of these complex structures (Figure 1). The integration of conventional Raman spectroscopy with HRTEM for complementary vibrational-structure analysis has confirmed the presence of different structural organizations of GO$_m$ sheet deformations modulated by carbon/oxygen atomic defect sites on both the surface and the expanded edges of vertical sheets (Figure 2). The direct electron imaging of atomic defects on the irregular surface (*D'* and 2D bands), and the abundant defects at the edges of vertical sheets (broad *D** band), provides more information when complemented with the sensitive Raman spectra. The assembling formations involving twisting (2D band), wrinkling (*D+D'* band), folding (D band), and intercalation (blue-shifted G band) of the irregular GO$_m$ sheets have been validated by high-resolution imaging. In this regard, the sensitive vibrational modes analysis validates the chemical actions of both *sp^2* hybridization involving bending of hydrogenated-oxide functionality groups (G and *D** bands), and *sp^3* sites localized at the observed expanded edges (*D*** band).

The relevance of vibrational-structure characterization is also evident in the investigation of eumelanin superstructures, which showed behaviour of the Raman spectra related to carbon, oxygen, hydrogen (and nitrogen) vibrational bonds. Indeed, the corresponding broadening of D band (associated with an intrinsic high-disorder of the system) and G band (an indicator of

irregular stacking structure), which were similar in frequency as the GO_m Raman bands, represent the dominant vibrational modes. These analytical results are quantitatively validated for the first time through high resolution nanodiffraction/imaging, confirming the poor structural character of the eumelanin units as predicted by Raman band analysis. The assembled superstructures have shown irregularly stacked nanosheets composed of very small nanocrystalline domains exhibiting distinct orientations in response to the order/disorder of the surrounding interactions (zig-zag and quasi-hexagonal lattice fringe shapes, Figure 3). Indeed, this finding strongly impacts on the phonon modes, which are strictly dependent on both the dimension and the random orientation ($[h,k,0]$) and random stacking ($[0,0,l]$) along the crystallographic axes, resulting in multi-resonance broadening of the Raman spectra bands.

In our efforts to create manipulated routes of the eumelanin units, we show that the micronized GO sheets exhibited notable control over the eumelanin units in aqueous solution at room temperature. For the first time, the eMel superstructures have demonstrated the ability to disassemble irregular nanosheets and reassemble into nanoscopic spherule particles, which also evolved in elongated shape, confined on the defective functional surface of the GO_m substrate (Figure 4). To overcome the limitation of HRTEM in imaging the crystalline lattices of soft eMel, the sensitive Raman spectra have clearly revealed changes of the $G_{GOm-eMel}$ and $D_{GOm-eMel}$ bands. This structural-vibrational change confirmed an increase in resonant shorter bonds (C=C and O-H) within eMel, followed by a decrease in the reactive functionality of GO_m substrate (Figure 1c-R_l). Furthermore, the red-shifted D^{**} band supports strong cooperation between eMel and GO_m, with the formation of spherule and elongated graphitic structures. In this regard, possible doping/intercalation of eMel in between GO_m sheets influenced the G and 2D bands, as confirmed by increased interlayers spacing observed through electron diffraction analysis (Figure 4d). With regards to manipulating the small biomaterials, the use of Raman-HRTEM complements existing strategies for revealing the strong affinity of self-assembling between carbon oxide layers and biological matter that does not require manual operations. This biocompatibility affinity suggests potential strategies for preserving the native state of small biomolecules upon adsorption onto appropriately engineered 2D materials in aqueous dispersion. The confirmed disassembling of nanostructured eMel with decreasing dimensional to nanometric units leads to size-dependent transition from continuous to discrete energy levels, thereby enhancing quantum yield. With regard to the hybrid integration, the electronic structures of the GO_m might be altered by inducing biomolecule-defect, actually creating a new bandgap tunable opening. Such variations in energy

Nanoscale Accepted Manuscript

levels may reduce the effective bandgap of the bulk GO_m-eMel hybrid material, significantly influencing their cross-correlated photophysical and photochemical properties. These effects will be highly relevant for practical applications in surface coatings, biosensing, and radiation protection.[47] Therefore, these results provide concrete information on ~~all~~ key scientific aspects in helping sustainable research towards the eventual control of ~~the~~ small biomolecules, which may have practical implications for graphene-based nanofabrication technologies with applications in environmental science and biomedicine.

4. Experimental Procedures

4.1 Sample Fabrication

Graphene oxide (GO) was synthesized using micronized natural graphite with 99.5% purity and a d50 of approximately 10 μm, following a modified Hummers method. The reagents used included sulfuric acid (H_2SO_4, 99%), potassium permanganate ($KMnO_4$, 99%), hydrogen peroxide (H_2O_2, 30%, Fmaia), and hydrochloric acid (HCl, Synth). The synthesis was primarily based on Hummer's method, ensuring that the temperature did not exceed 20 °C during the addition of H_2SO_4 and $KMnO_4$. In a beaker placed in an ice bath, 25 mL of concentrated H_2SO_4 and 1.0 g of graphite were first mixed under constant magnetic stirring. Afterwards, 3 g of $KMnO_4$ was slowly added to the mixture. After 3 hours of stirring, 50 mL of distilled water was added dropwise while maintaining the temperature below 50 °C, keeping the beaker in the ice bath. During this step, the dispersion color changed from black to dark brown. Next, 100 mL of distilled water was added, followed by the addition of 5 mL of H_2O_2 at room temperature to remove any excess $KMnO_4$ and stop the oxidation process. This change in the dispersion color from dark brown to greyish-green indicated the termination of the reaction. To purify the solution, 250 mL of a 30% v/v HCl solution was added, followed by centrifugation at 6000 rpm for 15 minutes. The samples were washed with distilled water and centrifuged multiple times until the pH of the dispersion reached approximately 6 (four washes). Chemical functionalization or doping of micronized GO were determinate and characterized using transmission FTIR and XPS spectra (see in Supplementary Information).

BSF eumelanin powder was provided by the manufacturer Insectta Pte. Ltd. for research purposes. The material is produced via a patented extraction process from the black soldier fly (*Hermetia illucens*).[48] The BSF eumelanin and GO_m were prepared separately by dissolving powder in distilled water with a concentration of 10 mg/mL. The GO_m-eMel suspensions suspensions were mixed all

at once, starting from the previous solutions, by mixing 1 mL of BSF eumelanin with 1 mL of GO$_m$ at room temperature.[49]

4.2 Raman Scattering Experiments

Raman spectra were collected at room temperature for all samples, which were deposited on FTO glass substrate by drop casting, in the range 100-3500 cm^{-1} using probing light source of 532 nm green laser with a 600 lines/mm diffraction grating and a 100x objective. The laser power was 10 mW or less to minimise damage to the samples. HORIBA IHR320 micro-Raman Scattering system (Horiba, Palaiseau, France) equipped with Olympus BXF41 an optical microscope model with 5x, 20x, 50x, 100x objectives (Olympus, Münster, Germany). After baseline correction and normalization, the contribution of the possible Raman scattering band was determined by curve deconvolution and peak fitting, using the Voigt deconvolution method on the entire Raman profile.[50] The deconvoluted peaks at 560 and 1098 cm-1 were excluded in the scattering analysis due to their FTO substrate contribution.

4.3 High-Resolution Transmission Electron Microscopy.

HR-TEM images were acquired using FEI Talos F200S Field Emission Gun (FEG) microscope operating @ 200 keV on samples deposited on Cu-support grid coated with a holey carbon amorphous film. Energy dispersive X-ray spectroscopy (EDX) compositional analysis maps were collected using a Super-X energy dispersive X-ray spectrometry system which includes two silicon drift detectors, couple to the microscope in the Scanning Transmission Electron Microscopy (STEM) mode, using spatial drift correction and a dwell time of 0.2 s. To avoid the occurrence of any fake structural information, we were forced to perform fast image acquisition using minimum dose techniques for preventing electron beam induced damage to the organic specie.[51] To observe the real possibility of strong molecular interactions of the hybrid system, the GO$_m$-eMel biomaterial with further dilution of distilled water was treated under soft sonication force capable of removing the biomolecules in excess, before observations with negative-staining HRTEM observations.[46]

Author contributions

Roberto Matassa: conceptualization, formal analysis, funding acquisition, investigation, methodology, resource, supervision, validation, visualization, writing – original draft, writing – review & editing. Sara Mattiello: conceptualization, formal analysis, investigation, writing – review

& editing. Gustavo Guerriero Candido Soares: investigation, writing – review & editing. Juan G. Lozano: funding acquisition, investigation, resource, validation, visualization, writing – review & editing. Ana M. Beltran: funding acquisition, validation, investigation, resource, writing – review & editing. Costantino Zazza and Nico Sanna: writing – review & editing. Jun Wei Phua: resource, writing – review & editing. Jose Mauricio Rosolen: funding acquisition, investigation, validation, visualization, resource, writing – review & editing. Andrea Di Cicco: funding acquisition, resource, writing – review & editing. Javad Rezvani: writing – review & editing. Roberto Gunnella: conceptualization, funding acquisition, investigation, methodology, resource, supervision, validation, writing – review & editing.

Data availability

All data generated or analyzed during this study are included in this published article and its ESI.

Conflicts of interest

Jun Wei Phua holds shares in Insectta Pte. Ltd., which owns patents related to the extraction of eumelanin from black soldier flies.

Acknowledgments

References

1. Karthick V.; Kumar L.; Shrestha L. K.; Kumar V. G.; Pranjali P., Kumar D.; Pal A. and Ariga K. Nanoarchitectonics horizons: materials for life sciences *Nanoscale* 14, 10630-10647, (2022). DOI: https://doi.org/10.1039/D2NR02293A

2. Campos M. T.; Pires L. S.; Magalhães F. D.; Oliveira M. J. and Pinto A. M. Self-assembled inorganic nanomaterials for biomedical applications. *Nanoscale* 17, 5526-5570, (2025). DOI: https://doi.org/10.1039/D4NR04537H.

3. Meredith P, Powell BJ, Riesz J, Nighswander-Rempel SP, Pederson MR, Moore EG. Towards structure-property-function relationships for eumelanin. *Soft Matter*.2(1),37-44, (2006). doi: 10.1039/b511922g.

4. Cheng J, Moss SC, Eisner M. X-ray characterization of melanins-II. *Pigment Cell Res.* 7(4), 263-73, (1994). doi: 10.1111/j.1600-0749.1994.tb00061.x.

5. Littrell K.C., Gallas J.M., Zajac G.W., Thiyagarajan P. Structural studies of bleached melanin by synchrotron small-angle X-ray scattering. *Photochem Photobiol.* 77(2), 115-120 (2003). doi: 10.1562/0031-8655(2003)077<0115:ssobmb>2.0.co;2

6. Powell B.J.; Baruah T.; Bernstein N.; Brake K.; McKenzie R.H.; Meredith P.; Pederson M.R. A first-principles density-functional calculation of the electronic and vibrational structure of the key melanin monomers. *J Chem Phys.* 120, 8608-8615, (2004). DOI: 10.1063/1.1690758. PMID: 15267788.

7. Paredes J. I. and Villar-Rodil S. Biomolecule-assisted exfoliation and dispersion of graphene and other two-dimensional materials: a review of recent progress and applications *Nanoscale* 8, 15389-15413, (2016). DOI: https://doi.org/10.1039/C6NR02039A.

8. Ferrari A. C.; Bonaccorso F.; Fal'ko V.; Novoselov K. S.; Roche S. et al. Science and technology roadmap for graphene, related two-dimensional crystals, and hybrid systems. *Nanoscale* 7, 4598-4810, (2015). DOI: https://doi.org/10.1039/C4NR01600A

9. Al-Shamery N.; Gong X.; Dosche C.; Gupta A.; Ming Tan M. W.; Phua J. W. & Lee P.S. Sustainable organic electrodes using black soldier fly-derived melanin for zinc-ion hybrid capacitors *Communications Materials* 5, 156, (2024). DOI: 10.1038/s43246-024-00602-4.

10. Dreyer D.R., Park S., Bielawski C.W., Ruoff R.S. The chemistry of graphene oxide. *Chem Soc Rev*. 39, 228-240, (2010). doi: 10.1039/b917103g.

11. Cançado L.G., Pimenta M.A., Neves B.R., Dantas M.S., Jorio A. Influence of the atomic structure on the Raman spectra of graphite edges. *Phys Rev Lett.* 93, 247401, (2004). doi: 10.1103/PhysRevLett.93.247401.

12. Meyer J.C.; Girit C.O.; Crommie M.F.; Zettl A. Imaging and dynamics of light atoms and molecules on graphene. *Nature* 454, 319-322, (2008). DOI: 10.1038/nature07094..

13. Politi S, Carcione R, Tamburri E, Matassa R, Lavecchia T, Angjellari M, Terranova ML. Graphene platelets from shungite rock modulate electropolymerization and charge storage mechanisms of soft-template synthetized polypyrrole-based nanocomposites. *Sci Rep.* 19;8(1):17045, (2018). doi: 10.1038/s41598-018-35415-2.

14. Cançado L. G., Jorio A., Ferreira E.H., Stavale F., Achete C.A., Capaz R.B., Moutinho M.V., Lombardo A., Kulmala T.S., Ferrari A.C. Quantifying defects in graphene via Raman spectroscopy at different excitation energies. *Nano Lett.* 11,3190-3196, (2011). doi: 10.1021/nl201432g.

15. Pimenta M.A., Dresselhaus G., Dresselhaus M.S., Cançado L.G., Jorio A., Saito R. Studying disorder in graphite-based systems by Raman spectroscopy *Phys Chem Chem Phys.* 9, 1276-1291, (2007). doi: 10.1039/b613962k.

16. Mostert A.B.; Mattiello S.; Li S.; Perna G.; Lasalvia M.; Ambrico P.F.; Paulin J.V.; Lima J.V.M.; Graeff C.F.O.; , Phua J.W.; Matta M.; Surman A.J.; Gunnella R.; Ambrico M. Exploring the chemistry and composition of black soldier fly eumelanin, a material for a circular economy *Mater. Adv.* 5, 8986-8999, (2024). DOI: 10.1039/d4ma00825a

17. Perna G., Lasalvia M., Capozzi V. Vibrational spectroscopy of synthetic and natural eumelanin *Polym. Int.* 65, 1323–1330 (2016). doi: 10.1002/pi.5182.

18. Tan P., Hu C., Dong J., Shen W. and Zhang B. Polarization properties, high-order Raman spectra, and frequency asymmetry between Stokes and anti-Stokes scattering of Raman modes in a graphite whisker *Phys. Rev. B* 64, 214301- 214313, (2001).

19. S. Cerra, T. A. Salamone, F. Sciubba, M. Marsotto, C. Battocchio, S. Nappini, F. A. Scaramuzzo, R. Li Voti, C. Sibilia, R. Matassa, A. M. Beltrán, G. Familiari, I. Fratoddi Study of the interaction mechanism between hydrophilic thiol capped gold nanoparticles and melamine in aqueous medium *Colloids Surf. B: Biointerfaces* 203, 111727, (2021). doi: 10.1016/j.colsurfb.2021.111727.

20. Matassa R, Familiari G, Battaglione E, Sibilia C, Leahu G, Belardini A, Venditti I, Fontana L, Fratoddi I. Electron microscopy reveals a soluble hybrid network of individual nanocrystals self-anchored by bifunctional thiol fluorescent bridges. *Nanoscale* 8(42),18161-18169, (2016). doi: 10.1039/c6nr06260a.

21. Li Voti, R.; Leahu, G.; Sibilia, C.; Matassa, R.; Familiari, G.; Cerra, S.; Salamone, T. A.; Fratoddi, I. Photoacoustics for Listening to Metal Nanoparticle Super-Aggregates. *Nanoscale Adv.* **2021**, *3*, 4692–4701. https://doi.org/10.1039/D1NA00333J.

22. Reina G., Tamburri E., Orlanducci S., Gay S., Matassa R., Guglielmotti V., Lavecchia T., Terranova M. L. Nanocarbon surfaces for biomedicine *Biomatter,* 4, e28537, (2014). https://doi.org/10.4161/biom.28537.

23. Matassa R, Orlanducci S, Reina G, Cassani MC, Passeri D, Terranova ML Structural and morphological peculiarities of hybrid Au/nanodiamond engineered nanostructures. *Sci Rep.* 12, 6:31163, (2016). doi: 10.1038/srep31163.

24. Lee, A. Y.; Yang, K.; Anh, N. D.; Park, C.; Lee, S. M.; Lee, T. G.; Jeong, M. S. Raman Study of D* Band in Graphene Oxide and Its Correlation with Reduction. Appl. Surf. Sci. 536, 147990, (2021). DOI: 10.1016/j.apsusc.2020.147990.

25. Nakamizo M., and Tamai K. Raman spectra of the oxidized and polished surfaces of carbon *Carbon.* **22**(2), 197–198 (1984).

26. Kudin K.N., Ozbas B., Schniepp H.C., Prud'homme R.K., Aksay I.A., Car R. Raman spectra of graphite oxide and functionalized graphene sheets *Nano Lett.* 8, 36-41, (2008). doi: 10.1021/nl071822y.

27. Ferrari A. C. and Robertson J. Interpretation of Raman spectra of disordered and amorphous carbon *Phys. Rev. B* 61, 14095, (2000). doi.org/10.1103/PhysRevB.61.14095.

28. Robertson J. Amorphous carbon *Curr. Opin. Solid State Mater. Sci.* 1, 557-561, (1996). doi.org/10.1016/S1359-0286(96)80072-6.

29. Adamopoulos G., Gilkes K.W.R., Robertson J., Conway N.M.J., Kleinsorge B.Y., Buckley A., Batchelder D.N. Ultraviolet Raman characterisation of diamond-like carbon films *Diam. Relat. Mater.* 8, 541–544, (1999).

30. Kawashima Y., and Katagiri G., Fundamentals, overtones, and combinations in the Raman spectrum of graphite. *Phys. Rev. B.* **52**(14),10053 (1995). doi: 10.1103/PhysRevB.52.10053.

31. Ferrari, A. C.; Basko, D. M. Raman Spectroscopy as a Versatile Tool for Studying the Properties of Graphene. *Nat. Nanotechnol* 8, 235–246, (2014).

32. Kim K., Coh S., Tan L.Z., Regan W., Yuk J.M., Chatterjee E., Crommie M.F., Cohen M.L., Louie S.G., Zettl A. Raman spectroscopy study of rotated double-layer graphene: misorientation-angle dependence of electronic structure *Phys Rev Lett.* 108, 246103, (2012) doi: 10.1103/PhysRevLett.108.246103.

33. Zhao W., Tan P.H., Liu J., Ferrari A.C. Intercalation of few-layer graphite flakes with FeCl3: Raman determination of Fermi level, layer by layer decoupling, and stability *J Am Chem Soc.* 133, 5941-5946, (2011). doi: 10.1021/ja110939a.

34. Capozzi V., Perna G. , Gallone A., Biagi P. F., Carmone P., Fratello A., Guida G., Zanna P., Cicero R. J. Raman and optical spectroscopy of eumelanin films *J. Mol. Struc.* 744, 717-721, (2005). doi:10.1016/j.molstruc.2004.11.074.

35. Roldán M. L., Centeno S. A., Rizzo A. An improved methodology for the characterization and identification of sepia in works of art by normal Raman and SERS, complemented by FTIR, Py-GC/MS, and XRF J. Raman Spectrosc. 2014, 45, 1160–1171, (2014). doi:10.1002/jrs.4620.

36. Kaniyoor A.; Ramaprabhu S. A Raman spectroscopic investigation of graphite oxide derived graphene *AIP Advances* 2, 032183, (2012). doi: doi.org/10.1063/1.4756995.

37. S. Cerra, R. Matassa, A. M. Beltrán, G. Familiari, C. Battocchio, I. Pis, F. Sciubba, F. A. Scaramuzzo, A. Del Giudice, I. Fratoddi Insights about the interaction of methotrexate loaded hydrophilic gold nanoparticles: Spectroscopic, morphological and structural characterizations *Mat. Sci. and Eng. C*, 117, 111337 (2020). doi: 10.1016/j.msec.2020.111337.

38. Sasikumar D., Vinod K., Sunny J., Hariharan M. Exciton interactions in helical crystals of a hydrogen-bonded eumelanin monomer *Chem Sci.* 13(8) , 2331-2338 (2022). DOI: 10.1039/d1sc06755a.

39. Yang Z.Q., Verbeeck J., Schryvers D., Tarcea N., Popp J., Rösler W. TEM and Raman characterisation of diamond micro- and nanostructures in carbon spherules from upper soils. *Diam Relat Mater* 17, 937–943, (2008).

40. Endo M., Kim Y.A., Hayashi T., Muramatsu H., Terrones M., Saito R., Villalpando-Paez F., Chou S.G., Dresselhaus M.S. Nanotube coalescence-inducing mode: a novel vibrational mode in carbon systems *Small* 2(8-9):1031-1036, (2006). doi: 10.1002/smll.200600087

41. May P., Lazzeri M., Venezuela P., Herziger F., Callsen G., Reparaz J. S., Hoffmann A., Mauri F., and Maultzsch J. Signature of the two-dimensional phonon dispersion in graphene probed by double-resonant Raman scattering *Phys. Rev. B* 87, 075402, (2013). doi: 10.1103/PhysRevB.87.075402.

42. Graf D., Molitor F., Ensslin K., Stampfer C., Jungen A., Hierold C., Wirtz L. Spatially resolved Raman spectroscopy of single- and few-layer graphene. *Nano Lett.* 7(2), 238-242, (2007). doi: 10.1021/nl061702a.

43. Ravagnan L., Siviero F., Lenardi C., Piseri P., Barborini E., Milani P., Casari C.S., Li Bassi A., Bottani C.E. Cluster-beam deposition and in situ characterization of carbyne-rich carbon films. *Phys Rev Lett.* ;89, 285506. doi: 10.1103/PhysRevLett.89.285506.

44. Hernandez Y., Nicolosi V., Lotya M., Blighe F.M., Sun Z., De S., McGovern I.T., Holland B., Byrne M., Gun'Ko Y.K., Boland J.J., Niraj P., Duesberg G., Krishnamurthy S., Goodhue R., Hutchison J., Scardaci V., Ferrari A.C., Coleman J.N. High-yield production of graphene by liquid-phase exfoliation of graphite. *Nat Nanotechnol.* 9, 563-568, (2008). doi: 10.1038/nnano.2008.215.

45. Lee J., Kim C., Cheong J. Y. , Kim I.D. An angstrom-level d-spacing control of graphite oxide using organofillers for high-rate lithium storage Chem 8, 2393–2409, (2022). doi: 10.1016/j.chempr.2022.05.002.

46. Maciel I.O., Anderson N., Pimenta M.A., Hartschuh A., Qian H., Terrones M., Terrones H., Campos-Delgado J., Rao A.M., Novotny L., Jorio A. Electron and phonon renormalization near charged defects in carbon nanotubes. *Nat Mater.* 7(11), 878-83, (2008). doi: 10.1038/nmat2296.

47. Li D, Zhang W, Yu X, Wang Z, Su Z, Wei G. When biomolecules meet graphene: from molecular level interactions to material design and applications. *Nanoscale* 8, 19491-19509, (2016). doi: 10.1039/c6nr07249f.

48. J.W. Phua, Ottenheim C, US Patent No. US 20230127563A1, 2023.

49. Ambrico M., Mostert A.B., Ambrico P.F., Phua J. W., Mattiello S. and Gunnella R. Exploring ion mobility mechanisms in poly indolequinone polymers: a case study on black soldier fly melanin J. Phys. D: Appl. Phys. 57, 265303, (2024). doi: 10.1088/1361-6463/ad3765.

50. K. S. Lee, Z. Landry, F. C. Pereira, M. Wagner, D. Berry, W. E. Huang, G. T. Taylor, J. Kneipp, J. Popp, M. Zhang, J. X. Cheng and R. Stocker Raman microspectroscopy for microbiology *Nat Rev Methods Primers* 1, 79, (2021).

51. Matassa R., Gatti M., Crociati M., Brunelli R., Battaglione E., Papi M., De Spirito M., Nottola S.A., Familiari G. Self-assembly of glycoprotein nanostructured filaments for modulating extracellular networks at long range. *Nanoscale* 15, 17972-17986, (2023). doi: 10.1039/d3nr02644b.

All data generated or analyzed during this study are included in this published article and its ESI.

Nanoscale Accepted Manuscript